Mechanical, Structural and Electronic Properties of CO$_2$ Adsorbed Graphitic Carbon Nitride (g-C$_3$N$_4$) under Biaxial Tensile Strain

Li-Hua Qu [1,*], **Chong-Gui Zhong** [1], **Peng-Xia Zhou** [1] and **Jian-Min Zhang** [2]

[1] School of Science, Nantong University, Nantong 226019, China; chgzhong@ntu.edu.cn (C.-G.Z.); ntzhoupx@ntu.edu.cn (P.-X.Z.)
[2] College of Physics and Information Technology, Shaanxi Normal University, Xi'an 710062, China; jmzhang@snnu.edu.cn
* Correspondence: qulihua05@163.com

Abstract: We investigate mechanical, structural and electronic properties of CO$_2$ adsorbed graphitic carbon nitride (g-C$_3$N$_4$) system under biaxial tensile strain via first-principles calculations. The results show that the stress of CO$_2$ adsorbed g-C$_3$N$_4$ system increases and then decreases linearly with the increasing biaxial strain, reaching maximum at 0.12 strain. This is primarily caused by the plane N–C stretching of the g-C$_3$N$_4$. Furthermore, both the Perdew-Burke-Ernzerhof (PBE) and Heyd- Scuseria-Ernzerhof screened hybrid functional (HSE06) band gaps show direct-indirect transitions under biaxial tensile strain and have the maximum also at 0.12 strain. It is found that there is large dipole transition matrix element around Γ point, leading high optical absorption coefficients of the deformed adsorption system, which would be of great use for the applications of new elastic nanoelectronic and optoelectronic devices.

Keywords: CO$_2$; graphitic carbon nitride; strain; first-principles

1. Introduction

The greenhouse effect is the rise in temperature caused by the rapid energy consumption on the global scale. This situation commits us to exploring effective methods for developing renewable energy. One of the most promising methods is to boost photocatalytic CO$_2$ reduction into hydrocarbon solar fuels, which can solve energy crisis and simultaneously protect our environment [1–4]. In 1979 [5], Inoue and his coworkers reported photocatalytic CO$_2$ reduction fuels using several semiconductors. After this, wide band gap semiconductor materials for CO$_2$ photoreduction have been studied, including CuO, TiO$_2$ and NiO and some metal sulfides [6–9]. All these photocatalysts are usually inorganic semiconductors, which distinguishes from the natural enzymes in plant tissues. Hence it is noted that biomimetic photocatalytic materials for photocatalytic CO$_2$ reduction are widely studied [10,11]. As an organic semiconductor photocatalyst, graphitic carbon nitride (g-C$_3$N$_4$) has attracted much attention due to its visible-light activity, nontoxic resource, low-cost, promising applications in water splitting and what matters more is its appropriate band positions for CO$_2$ photoreduction [2,12,13].

Adsorption of CO$_2$ on the g-C$_3$N$_4$ is critical for the photocatalytic activity [14,15]. In addition, the adsorption structure, stability and strength are very important for the electronic behavior. In recent years, the research on CO$_2$ photoreduction by g-C$_3$N$_4$- based photocatalysts has aroused a lot of concern and discussion [2,12–14]. For instance, sulfur doped g-C$_3$N$_4$ are designed to improve photocatalytic CO$_2$ reduction performance [15]. g-C$_3$N$_4$ nanocomposites have been designed for effective CO$_2$ photoreduction, since the e−/h+ separation efficiency has risen, including Cu-NPs/g-C$_3$N$_4$ [14], g-C$_3$N$_4$/Ag/m-CeO$_2$ [16] and Sr$_2$Ta$_2$O$_7$/S-doped g-C$_3$N$_4$ [17] heterojunctions.

In addition, Caux et al. [18] have studied Pt-g-C_3N_4 for CO_2 photoreduction to improve the catalytic performance ascribed to the charge-separation efficiency. Different from these composite photocatalysts prepared by expensive metal salts, the preparation of pristine g-C_3N_4 photocatalyst can be made facilely by thermally polycondensing the cheap N-rich precursors, such as cyanamide, dicyanamide, urea and melamine [19,20]. The outstanding characteristics of g-C_3N_4 can be very beneficial in water splitting, CO_2 photoreduction, catalytic organic synthesis, organic contaminants purification and fuel cells [20]. In previous years, there are several excellent research on the g-C_3N_4 preparation and applications [21,22]. In addition, all these studies result from the changes of the local atomic structure, electronic states and mechanical behavior of materials. Furthermore, strain is almost inevitable and the strain effects on the structural and electronic properties of two-dimensional materials have been studied for decades. Sometimes, strain is intentionally applied to improve mobility, as in the strained silicon technology, which is used in modern microelectronics [23]. Thus, it is crucial to understand how the strain affects the further deformation, electronic structures and mechanical properties for the CO_2 adsorbed g-C_3N_4.

In present paper, we investigate the mechanical, structural and electronic properties of biaxial tensile strain tuned CO_2 adsorbed g-C_3N_4 system based on first-principles density functional theory (DFT) [24,25] calculations. The rest of the paper is organized as follows. Section 2 shows the calculation methods and optimized structures of CO_2 adsorbed g-C_3N_4 system. Section 3 is devoted to the effects of biaxial strain regulated mechanical, structural and electronic properties of the adsorption system. Section 4 presents the conclusions.

2. Computational Methods

Our calculations are performed using DFT with the generalized gradient approximation of Perdew-Burke-Ernzerhof (GGA-PBE) form [26], as implemented in the Vienna ab initio Simulation Package (VASP) code [24–29]. In addition, the projector augmented wave (PAW) [26] approach is derived. $5 \times 5 \times 1$ Monkhorst-Pack k-point meshes [30] are used to sample the Brillouin zone. The PBE and HSE06 exchange-correlation functionals are adopted. The wave functions are expanded in a plane-wave basis set with an energy cutoff of 450 eV. The total energy and atomic forces are converged to 10^{-6} eV and 0.02 eV/Å. The biaxial strain can be calculated with the following equation [31]:

$$\varepsilon = (a - a_0)/a_0 = (b - b_0)/b \tag{1}$$

where a, b and a_0, b_0 are the deformed (stretched or shrunken) and initial equilibrium lattice constants of unit cell. Figure 1a,b show the top and side views of unit cell for the CO_2 adsorbed g-C_3N_4 system, respectively, which are represented by the dashed black parallelogram. The green, yellow and red balls represent C, N and O atoms, respectively. In addition, the orientation of biaxial tensile strain is marked with black arrows. The unit cell of pristine g-C_3N_4 contains three types of N atoms and two types of C atoms (N1, N2, N3, C1 and C2), therefore there are four kinds of N–C bonds (N1–C1, C1–N2, N2–C2 and N3–C2) (shown in Figure 1). The optimized lattice constant of pristine g-C_3N_4 turns out to be 7.15 Å, which is consistent with the previous studies [32,33]. We investigate optimization of adsorption system under biaxial tensile strain from 0 to 0.2 with an increment of 0.01 per step. Upon CO_2 adsorption, the planar g-C_3N_4 structure of becomes buckled (puckered). Previous research has shown that CO_2 prefers to adsorb nearly parallel to the g-C_3N_4 plane [34]. In this work, gas-phase calculations have proven useful because they provide in an unperturbed way rather detailed insight into the elementary steps of numerous transformations mediated by the catalysts.
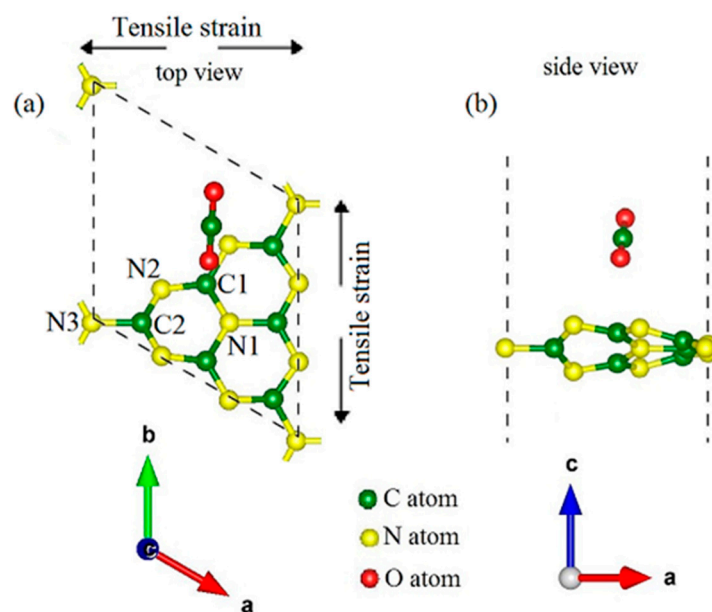
Figure 1. (**a**,**b**) are the top and side views of the optimized CO_2 adsorbed g-C_3N_4 (without strain) system within the unit cell, respectively, which is represented by the dashed black parallelogram. The green, yellow and red balls represent C, N and O atoms, respectively. In addition, the orientation of biaxial tensile strain is signed with black arrows. For the pristine g-C_3N_4, there are three types of N and two types of C (N1, N2, N3, C1 and C2).

3. Results

3.1. Mechanical and Structural Properties

The stress-strain relations of CO_2 adsorbed g-C_3N_4 system are displayed in Figure 2a. The stress increases almost linearly with the increasing biaxial tensile strain and reaches maximum at about 0.12 strain, then it suddenly drops as the strain increases. The phenomenon of linear elasticity in the CO_2 adsorbed g-C_3N_4 system suggests that its stretchability may not reach high values, because its stretching of bonds have limitations. In order to study the deformation mechanism in more details, we display the bond lengths-strain curves in Figure 2b,c. It has been found that the C–O bond lengths change relatively little with the increasing strain, so we only consider the N–C bonds here. It can be noticed that the outside N3–C2 bond (signed in Figure 1) is stretched more than the inner ones (N1–C1, N2–C1 and N2–C2 in Figure 1), because of the stronger stress concentration around the pore tip. From Figure 2b, we can see that the growth of all the inner bonds (N1–C1, N2–C1 and N2–C2) start to fall at 0.12 strain and show opposite changes of up and down at around 0.16 strain, resulting the decrease of stress-strain curve in Figure 2a. However, the outside N3–C2 bond continues to grow until strain of 0.18, as shown in Figure 2c.

In Figure 3a,b, we draw the CO_2 adsorbed g-C_3N_4 system along with its the electron localization function (ELF) [35] contour at biaxial strain of 0 and 0.12, and the ELF takes a value between 0 and 1. From the representation of the bond in the CO_2 adsorbed g-C_3N_4 system, it can be determined that the outside N3–C2 bond breaks at 0.12 and 0.2 strain. It is clear that the ELF contour agrees with the study of the bond length variations, suggesting that these bonds are very active under biaxial strain, because the ELF values of the inner bonds are about 0.85, showing integrity of covalent bonding. Figure 3c shows the adsorption energy-strain curve to analyze the stability, and the adsorption energy Eads is calculated by the following equation [36]:

$$E_{ads} = E_{total} - E_{g\text{-}C_3N_4} - E_{CO_2} \tag{2}$$

where E_{total}, $E_{g\text{-}C_3N_4}$ and E_{co_2} are the total energy of CO_2 adsorbed g-C_3N_4 system, g-C_3N_4 and CO_2, respectively. It is worthwhile to note that the adsorption of CO_2 on g-C_3N_4

is highly exothermic (negative adsorption energy) with strain less than 0.05, suggesting that g-C_3N_4 can be an excellent gas sensor. In addition, the adsorption energy increases with the increasing strain, indicating stronger interaction between CO_2 and g-C_3N_4. It is interesting to see that energy-strain curve has a maximum slope at 0.12 strain, which means that there is the biggest deformation. Furthermore, the adsorption energy increases almost quadratically with increasing biaxial strain, showing an elastic behavior rather than a viscous one. This study also demonstrates that the CO_2 adsorbed g-C_3N_4 system without strain is more stable. This is because the tensile strain weakens the bonds of the CO_2 adsorbed g-C_3N_4 system, resulting in higher chemical reactivity. This distinct behavior can be ascribed to the adsorption configuration and charge transfer, which will be systematically discussed below.
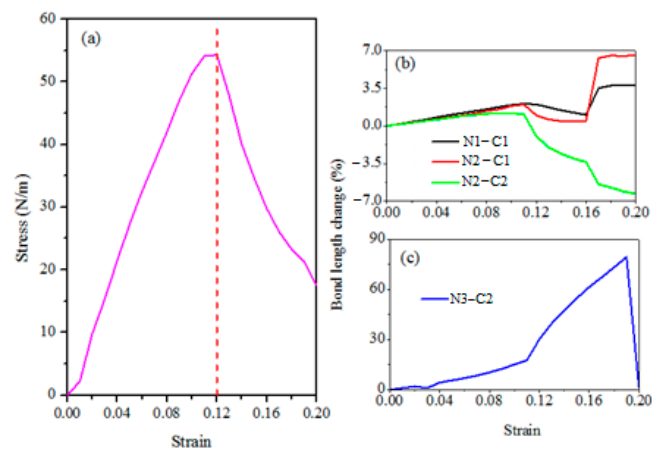
Figure 2. (**a**) the stress-strain curves of the CO_2 adsorbed g-C_3N_4 system. (**b**,**c**) are the N–C bond length change-strain curves.
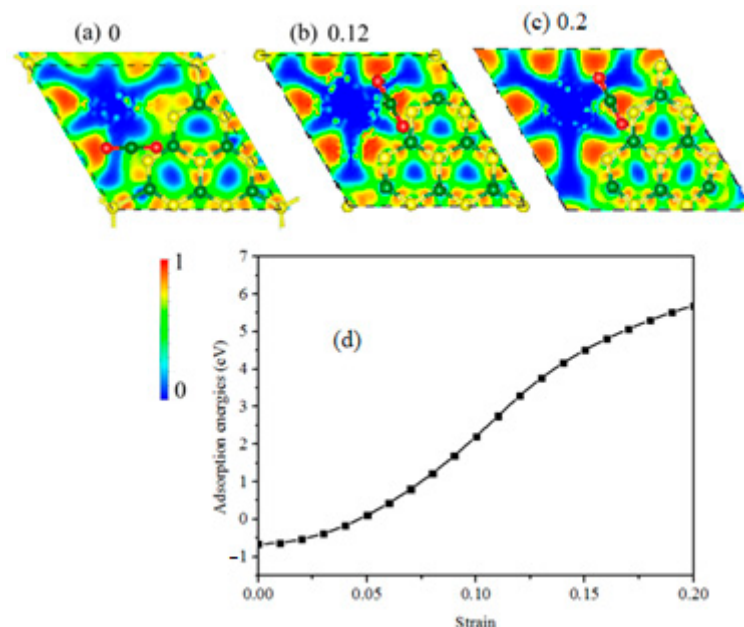
Figure 3. (**a**–**c**) are the atomic structures of the CO_2 adsorbed g-C_3N_4 system at 0, 0.12 and 0.2 strain, respectively. Contours illustrate the electron localization function (ELF) within the unit-cell. (**d**) shows the adsorption energy-strain curve of the CO_2 adsorbed g-C_3N_4 system.

3.2. Electronic Properties

Band structures calculated with PBE and HSE06 methods for CO_2 adsorbed g-C_3N_4 are shown in Figure 4a–d,i–l. The conduction band minimum (CBM) and valance band

maximum (VBM) band edge positions are denoted by the red and blue points, which are signed with A and B, respectively. Apparently, both PBE and HSE06 band gaps exhibit direct (K to K) to indirect (K to Γ) transitions at strain from 0 to 0.04 [see Figure 4a,b,i,j], and then turns to be direct (Γ to Γ) again at 0.12 strain [see Figure 4c,d,k,l]. Moreover, in Figure 4e–h, we plot the PBE high transition probabilities between the topmost valence and the lowest conduction bands, which are revealed by the squares of the dipole transition matrix elements [37], P^2, at all the k-points. It is found that the CO_2 adsorbed g-C_3N_4 system has large dipole transition matrix elements around Γ point, especially at 0.2 strain, indicating strong optical absorption coefficients of photons with energies near the bandgap, which is essential in optoelectronic applications. However, at any strain, the transition matrix amplitudes between band edges are very weak around the M and K points. The rich tunable properties show tremendous potential applications of the biaxial strained CO_2 adsorbed g-C_3N_4 system in elastic nanoelectronic and optoelectronic devices [38–40]. Moreover, comparison between the PBE and HSE06 shows that entire shape of band structures is independent of the functional. It is evident that the CBM and VBM are the same in PBE and HSE06. Both functionals show the same type (direct or indirect) of band structures. The band gap is the main difference of the band structures calculated using the two functionals. Therefore, one can qualitatively study the band structures of CO_2 adsorbed g-C_3N_4 with PBE instead of calculating the band in expensive HSE06. In addition, we conducted computational studies (PBE and HSE06) on defected g-C_3N_4 to elucidate how the biaxial strain is affected by CO_2 adsorption in the supporting information Figure S1. It is found that the band structures show metal states under 0 to 0.2 strain.
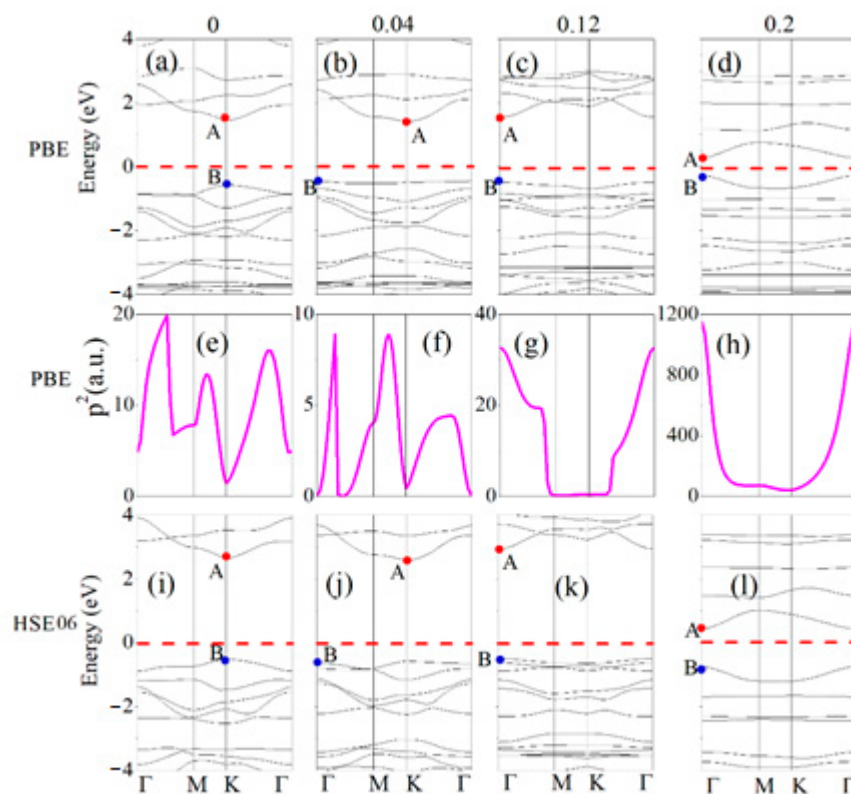
Figure 4. (**a–h**) are PBE calculated band structures and transition matrix elements of the CO_2 adsorbed g-C_3N_4 system at 0, 0.04, 0.12 and 0.2 strain. (**i–l**) are HSE06 calculated band structures of the CO_2 adsorbed g-C_3N_4 system at 0, 0.04, 0.13 and 0.2 strain. The CBM and VBM band edge positions denoted by the red and blue points, which are signed with A and B, respectively. The Fermi energy is set at zero energy and indicated by the red dashed line.

Figure 5 shows the PBE and HSE06 band gaps of CO_2 adsorbed g-C_3N_4 as a function of strain. The HSE06 can provide a better prediction of band gap in general. In addition,

the HSE06 band gaps are found to be higher than the PBE values under the same strain. Furthermore, the band gap-strain curves of the two methods have the same changing tendency that both methods reach the maximum at 0.12 strain, where the indirect-direct transition occurs, and it is the maximum tensile strength point of the CO_2 adsorbed g-C_3N_4 system.
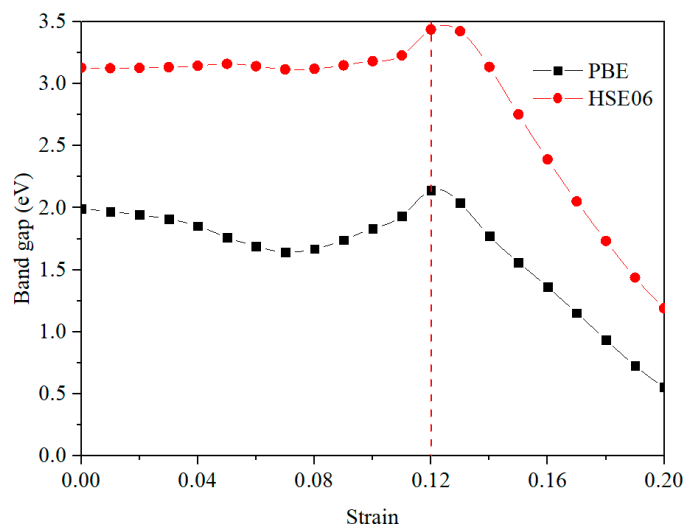
Figure 5. PBE and HSE06 band gap-strain curves of the CO_2 adsorbed g-C_3N_4 system.

4. Conclusions

In this work, we have investigated mechanical, structural and electronic properties of CO_2 adsorbed g-C_3N_4 system under biaxial tensile strain by performing first-principles calculations. The CO_2 adsorbed g-C_3N_4 system shows linear elasticity and has high strength at 0.12 strain, which is mainly induced by the stretching of N-C bonds in the g-C_3N_4 plane. In addition, the outside N-C bonds are stretched more than the inner ones. The unstrained CO_2 adsorbed g-C_3N_4 is more stable because of the bonds weakened by the stretching strain. Both the PBE and HSE06 band gaps exhibit direct- indirect transitions under biaxial tensile strain and reach maximum at 0.12 strain. There are large dipole transition matrix elements around Γ point, showing high optical absorption coefficients, which would be beneficial to the applications of elastic nanoelectronic and optoelectronic devices.

Conflicts of Interest: The authors declare no conflict of interest.

References

1. Nam, S.; Jeong, Y.J.; Park, C.E.; Jang, J. Enhanced gas barrier properties of graphene-TiO_2 nanocomposites on plastic substrates assisted by UV photoreduction of graphene oxide. *Org. Electron.* **2017**, *48*, 323–329. [CrossRef]
2. Raganati, F.; Ammendola, P. Sound-assisted fluidization for temperature swing adsorption and calcium looping: A review. *Materials* **2021**, *14*, 672. [CrossRef] [PubMed]
3. Barroso-Bogeat, A.; Blanco, G.; Pérez-Sagasti, J.J.; Escudero, C.; Pellegrin, E.; Herrera, F.C.; Pintado, J.M. Thermocatalytic CO_2 conversion over a nickel-loaded ceria nanostructured catalyst: A nap-xps study. *Materials* **2021**, *14*, 711. [CrossRef] [PubMed]
4. Šupić, S.; Malešev, M.; Radonjanin, V.; Bulatović, V.; Milović, T. Reactivity and pozzolanic properties of biomass ashes generated by wheat and soybean straw combustion. *Materials* **2021**, *14*, 1004. [CrossRef] [PubMed]
5. Inoue, T.; Fujishima, A.; Konishi, S.; Honda, K. Photoelectrocatalytic reduction of carbon dioxide in aqueous suspensions of semiconductor powders. *Nature* **1979**, *277*, 637–638. [CrossRef]
6. Shekaaria, A.; Jafaria, M. Unveiling the first post-graphene member of silicon nitrides: A novel 2D material. *Comput. Mater. Sci.* **2020**, *180*, 109693. [CrossRef]
7. Jantarasorn, N.; Mekasuwandumrong, O.; Kelly, P.; Praserthdam, P. Reactive magnetron sputter deposition of copper on TiO_2 support for photoreduction of CO_2 to CH_4. *IOP Conf. Ser. Mater. Sci. Eng.* **2019**, *559*, 012017. [CrossRef]
8. Han, C.; Zhang, R.; Ye, Y.; Wang, L.; Ma, Z.; Su, F.; Xie, H.; Zhou, Y.; Wong, P.K.; Ye, L. Chainmail co-catalyst of NiO shell-encapsulated Ni for improving photocatalytic CO_2 reduction over g-C_3N_4. *J. Mater. Chem. A* **2019**, *7*, 9726–9735. [CrossRef]
9. Suzuki, T.M.; Takayama, T.; Sato, S.; Iwase, A.; Kudo, A.; Morikawa, T. Enhancement of CO_2 reduction activity under visible light irradiation over Zn-based metal sulfides by combination with Ru-complex catalysts. *Appl. Catal. B-Environ.* **2018**, *224*, 572–578. [CrossRef]
10. Tseng, I.H.; Kang, L.H.; Chang, P.Y.; Tsai, M.H.; Yeh, J.M.; Yang, T.I. Biomimetic polyimide-supported cuprous oxide photocatalytic film with tunable hydrophobicity, improved thermal stability, and photocatalytic activity toward CO_2 reduction. *ACS Omega* **2019**, *4*, 1636–1644. [CrossRef]
11. Li, N.; Liu, J.; Liu, J.J.; Dong, L.Z.; Xin, Z.F.; Teng, Y.L.; Lan, Y.Q. Adenine components in biomimetic metal-organic frameworks for efficient CO_2 photoconversion. *Angew. Chem.* **2019**, *131*, 5191–5516.
12. Ma, W.; Wang, N.; Guo, Y.; Yang, L.; Lv, M.; Tang, X.; Li, S. Enhanced photoreduction CO_2 activity on g-C_3N_4: By synergistic effect of nitrogen defective-enriched and porous structure, and mechanism insights. *Chem. Eng. J.* **2020**, *388*, 124288. [CrossRef]
13. Wang, H.; Li, H.; Chen, Z.; Li, J.; Li, X.; Huo, P.; Wang, Q. TiO_2 modified g-C_3N_4 with enhanced photocatalytic CO_2 reduction performance. *Solid State Sci.* **2020**, *100*, 106099. [CrossRef]
14. Sun, Z.; Fang, W.; Zhao, L.; Wang, H. 3D porous Cu-NPs/g-C_3N_4 foam with excellent CO_2 adsorption and schottky junction effect for photocatalytic CO_2 reduction. *Appl. Surf. Sci.* **2020**, *504*, 144347. [CrossRef]
15. Gupta, B.; Gupta, A.K.; Ghosal, P.S.; Tiwary, C.S. Photo-induced degradation of bio-toxic Ciprofloxacin using the porous 3D hybrid architecture of an atomically thin sulfur-doped g-C_3N_4/ZnO nanosheet. *Environ. Res.* **2020**, *183*, 109154. [CrossRef]
16. Wang, H.; Guan, J.; Li, J.; Li, X.; Ma, C.; Huo, P.; Yan, Y. Fabricated g-C_3N_4/Ag/m-CeO_2 composite photocatalyst for enhanced photoconversion of CO_2. *Appl. Surf. Sci.* **2020**, *506*, 144931. [CrossRef]
17. Zeng, W.; Bian, Y.; Cao, S.; Zhu, A.; Qiao, L.; Ma, Y.; Tan, P.; Ma, Q.; Dong, R.; Pan, J. Construction of two dimensional $Sr_2Ta_2O_7$/S-doped g-C_3N_4 nanocomposites with Pt cocatalyst for enhanced visible light photocatalytic performance. *Appl. Surf. Sci.* **2019**, *478*, 334–340. [CrossRef]
18. Caux, M.; Fina, F.; Irvine, J.T.S.; Idriss, H.; Howe, R. Impact of the annealing temperature on Pt/g-C_3N_4 structure, activity and selectivity between photodegradation and water splitting. *Catal. Today* **2017**, *287*, 182–188. [CrossRef]
19. Yan, S.C.; Li, Z.S.; Zou, Z.G. Photodegradation Performance of g-C_3N_4 Fabricated by directly heating melamine. *Langmuir* **2009**, *25*, 10397–10401. [CrossRef] [PubMed]
20. Dong, F.; Wu, L.W.; Sun, Y.J.; Fu, M.; Wu, Z.B.; Lee, S.C. Efficient synthesis of polymeric g-C_3N_4 layered materials as novel efficient visible light driven photocatalysts. *J. Mater. Chem.* **2011**, *21*, 15171–15174. [CrossRef]
21. Gong, Y.G.; Li, M.M.; Wang, Y. Carbon nitride in energy conversion and storage: Recent advances and future prospects. *ChemsusChem* **2015**, *8*, 931–946. [CrossRef]
22. Wang, Y.; Wang, X.C.; Antonietti, M. Polymeric graphitic carbon nitride as a heterogeneous organocatalyst: From photochemistry to multipurpose catalysis to sustainable chemistry. *Angew. Chem. Int. Ed.* **2012**, *51*, 68–89. [CrossRef]
23. Zhang, S.; Yan, Z.; Li, Y.; Chen, Z.; Zeng, H. Atomically thin arsenene and antimonene: Semimetal-semiconductor and indirect-direct band-gap transitions. *Angew. Chem. Int. Ed.* **2015**, *54*, 3155–3158. [CrossRef]
24. Kresse, G.; Hafner, J. Ab initio molecular dynamics for liquid metals. *Phys. Rev. B* **1993**, *47*, 558–561. [CrossRef]
25. Kresse, G.; Furthmüller, J. Efficient iterative schemes for ab initio total-energy calculations using a plane-wave basis set. *Phys. Rev. B* **1996**, *54*, 11169–11186. [CrossRef]

26. Perdew, J.P.; Burke, K.; Ernzerhof, M. Generalized gradient approximation made simple. *Phys. Rev. Lett.* **1996**, *77*, 3865–3868. [CrossRef]

27. Kresse, G.; Hafner, J. Ab initio molecular-dynamics simulation of the liquid-metal-amorphous-semiconductor transition in germanium. *Phys. Rev. B* **1994**, *49*, 14251–14269. [CrossRef] [PubMed]

28. Kresse, G.; Furthmüller, J. Efficiency of ab-initio total energy calculations for metals and semiconductors using a plane-wave basis set. *Comput. Mat. Sci.* **1996**, *6*, 15–50. [CrossRef]

29. Kresse, G.; Joubert, D. From ultrasoft pseudopotentials to the projector augmented-wave method. *Phys. Rev. B* **1999**, *59*, 1758–1775. [CrossRef]

30. Monkhorst, H.J.; Pack, J.D. Special points for Brillonin-zone integrations. *Phys. Rev. B* **1976**, *13*, 5188–5192. [CrossRef]

31. Qu, L.H.; Yu, J.; Mu, Y.L.; Fu, X.L.; Zhong, C.G.; Min, Y.; Zhou, P.X.; Zhang, J.M.; Zou, Y.Q.; Lu, T.S. Strain tunable structural, mechanical and electronic properties of monolayer tin dioxides and dichalcogenides SnX_2 (X = O, S, Se, Te). *Mater. Res. Bull.* **2019**, *119*, 110533. [CrossRef]

32. Zhu, B.; Zhang, J.; Jiang, C.; Cheng, B.; Yu, J. First principle investigation of halogen-doped monolayer g-C_3N_4 photocatalyst. *Appl. Catal. B Environ.* **2017**, *207*, 27–34. [CrossRef]

33. Cui, J.; Liang, S.; Wang, X.; Zhang, J. First principle modeling of oxygen-doped monolayer graphitic carbon nitride. *Mater. Chem. Phys.* **2015**, *161*, 194–200. [CrossRef]

34. Zhu, B.; Zhang, L.; Xu, D.; Cheng, B.; Yu, J. Adsorption investigation of CO_2 on g-C_3N_4 surface by DFT calculation. *J. CO_2 Util.* **2017**, *21*, 327–335. [CrossRef]

35. Silvi, B.; Savin, A. Classification of chemical-bonds based on topological analysis of electron localization functions. *Nature* **1994**, *371*, 683–686. [CrossRef]

36. Ni, J.; Quintana, M.; Song, S. Adsorption of small gas molecules on transition metal (Fe, Ni and Co, Cu) doped graphene: A systematic DFT study. *Physica E* **2020**, *116*, 113768. [CrossRef]

37. Maughan, A.E.; Ganose, A.M.; Bordelon, M.M.; Miller, E.M.; Scanlon, D.O.; Neilson, J.R. Defect tolerance to intolerance in the vacancy-ordered double perovskite semiconductors Cs_2SnI_6 and Cs_2TeI_6. *J. Am. Chem. Soc.* **2016**, *138*, 8453–8464. [CrossRef] [PubMed]

38. Zhou, Y.; Zhang, L.; Tao, S. Mesoporous ZrO_2 Nanopowder catalysts for the synthesis of 5-hydroxymethylfurfural. *ACS Appl. Nano Mater.* **2019**, *2*, 3848. [CrossRef]

39. Bayan, S.; Gogurla, N.; Midya, A.; Singha, A.; Ray, S.K. Plasmon mediated enhancement and tuning of optical emission properties of two dimensional graphitic carbon nitride nanosheets. *Nanotechnology* **2017**, *28*, 485204. [CrossRef]

40. Bayan, S.; Midya, A.; Gogurla, N.; Singha, A.; Ray, S.K. Origin of modified luminescence response in reduced graphitic carbon nitride nanosheets. *J. Phys. Chem. C* **2017**, *121*, 19383. [CrossRef]